Room-Temperature $CsPbBr_3$ Mixed Polariton States

VINCENT FORSTER,[1,2,3,4] SALVADOR ESCOBAR GUERRERO,[5] HUGO ALBERTO LARA-GARCÍA,[5] JEAN-FRANÇOIS BRYCHE,[1,3,4] ROCÍO NAVA,[6] DENIS MORRIS,[1,2,3,4] AND JORGE-ALEJANDRO REYES-ESQUEDA[1,5,*]

[1]*Faculté des Sciences, Université de Sherbrooke, J1K 2R1 Sherbrooke, QC, Canada*
[2]*Institut Quantique, Université de Sherbrooke, J1K 2R1 Sherbrooke, QC, Canada*
[3]*Laboratoire Nanotechnologies Nanosystèmes (LN2)-IRL3463, CNRS, Université de Sherbrooke, Université Grenoble Alpes, École Centrale de Lyon, INSA Lyon, J1K 0A5 Sherbrooke, QC, Canada*
[4]*Institut Interdisciplinaire d'Innovation Technologique (3IT), Université de Sherbrooke, 3000 Boulevard de l'Université, J1K 0A5 Sherbrooke, QC, Canada*
[5]*Instituto de Física, Universidad Nacional Autónoma de México, Circuito de la Investigación Científica, Ciudad Universitaria, Coyoacán, 04510, Ciudad de México, México*
[6]*Instituto de Energías Renovables, Universidad Nacional Autónoma de México, Privada Xochicalco s/n, Temixco, Morelos, 62580, México*
**reyes@fisica.unam.mx*

Abstract: Light-matter interactions are known to lead to the formation of polariton states through what is called strong coupling, allowing the formation of two hybrid states usually tagged as Upper and Lower Polaritons. Here, we consider a similar interaction between excitons and photons in the realm of strong interactions, with the difference that it enables us to obtain a mixed-polariton state. In this case, the energy of this mixed state is found between the energies of the exciton state and the cavity mode, resulting in an imaginary coupling coefficient related to a specific class of singular points. These mixed states are often considered unobservable, although they are predicted well when the dressed states of a two-level atom are considered. However, intense light confinement can be obtained by using a Bound State in the Continuum, reducing the damping rates, and enabling the observation of mixed states resulting from the correct kind of exceptional point giving place to strong coupling. In this study, using the Transfer Matrix Method, we simulated cavities made of porous silicon coupled with $CsPbBr_3$ perovskite quantum dots to numerically observe the mixed states as well as experimentally, by fabricating appropriate samples. The dispersion relation of the mixed states is fitted using the same equation as that used for strong coupling but considering a complex coupling coefficient, which can be directly related to the appropriate type of exceptional point.

1. Introduction

First proposed around 1960 [1], strong coupling and the resulting bosonic quasiparticles known as polaritons have seen ever-increasing interest in the last few years, as several groups have raised their capacity to obtain and manipulate them by strongly controlling the parameters of the materials used to observe this coupling [2]. Following this achievement, new devices based on polariton Bose-Einstein condensation [3], polariton lasing and sensing [4,5], and modulating chemical reactions [6] have emerged, as well as all the possibilities for fabricating robust quantum technologies, given the drastic reduction in the future polariton-chip size and increase in their speed performance [7,8].

On the other hand, the ability to fabricate materials with specific parameters has also allowed observation of Bound States in the Continuum (BICs) in optics over the past decade [9]. BICs allow strong localization of energy in an open resonator coupled to a radiation

continuum [9-11], possessing infinite radiative lifetimes, thus enabling boundless enhancement of electric and magnetic fields through a divergent quality factor [12]. However, in practice, finite material extension, intrinsic absorption losses, fabrication defects, and structural disorders result in the fabrication of real-world leaky structures with quasi-BICs [13]. Two main types of quasi-BICs have attracted attention in recent years: symmetry-protected BICs and accidental BICs [14-16]. Given that a BIC can be explained by destructive interference, with only a discretized diffraction channel remaining open when photonic structures are on the subwavelength scale, the former is observed when the coupling of this channel to free space ceases owing to symmetry mismatch, whereas the latter can be observed by continuous parameter tuning [12,17].

The presence of BICs goes hand-in-hand with non-Hermitian physics because an open resonator implies a complex system with losses. In principle, a non-Hermitian system shows real eigenvalues if its Hamiltonian satisfies the conditions for parity-time (PT) symmetry [18]. However, in these systems, there are regions where symmetry is either preserved and broken, resulting in the existence of Exceptional Points (EPs) and the degeneracy of the Hamiltonian eigenfunctions and their complex eigenvalues [19]. This coalescence of eigenvalues implies that the Hamiltonian can no longer be diagonalized. In these cases, the system can be physically manipulated to lie either at or around the EP singularity [20]. In this context, optics and photonics have become natural domains for the experimental observation and use of these singularities [21,22].

BICs are often associated with emissive systems that improve or modify their emission properties. In this regard, perovskite nanocrystals have recently attracted attention owing to their potential applications in photovoltaic cells, light-emitting diodes, and tunable single-photon sources [23-27]. Similarly, the search for strong excitonic effects, low-temperature processing, and simple scalability, while allowing strong light-matter interactions, has also attracted significant interest in these materials to study room-temperature exciton-polariton formation [28-31]. In parallel, there is a growing interest in using porous silicon (p-Si) in biosensing and photonic applications, including strong coupling [32-39]. Indeed, porous silicon is a versatile nanoplatform thanks to the coral-like morphology produced by the electrochemical etching of crystalline silicon (c-Si). When extremely porous, light can be emitted because of the quantum confinement of charge carriers in the nanostructure as the p-Si skeleton thickness is reduced to a few nanometers (<4.3 nm, exciton Bohr radius) with the participation of surface states [40]. In addition, given that the etching process is self-limiting and primarily occurs at the pore tips, it opens the possibility of fabricating multilayered porous structures with a high contrast index between the porous layers, good interface quality, and a large surface area (540-840 m^2/cm^3).

In this work, we discuss the theoretical frameworks used first to calculate the photonic response of the coupled system, corresponding to the p-Si photonic cavity and the $CsPbBr_3$ perovskite quantum dots (QDs), and then the model to calculate the coupling between them, that is, the fitting of the corresponding dispersion relation. In this scope, we discuss how the presence of BIC modes allows the manifestation of related Exceptional Points, which gives rise to strong coupling such that mixed polaritonic states can be observed. We then present our simulation results for a wide range of related parameters, based on the corresponding empirical parametrization equation. From there, it follows naturally the fitting of the corresponding dispersion relations by considering the singularities resulting from the presence of BICs and EPs, that is, an imaginary coupling coefficient. We then discuss the band structure of the coupled system and topological charge of the mixed polaritonic states, showing how this topological charge reinforces the presence of the imaginary coefficient. Finally, we give preliminary experimental evidence of mixed polaritons for some associated parameters.

2. Methods and protocols

2.1 Transfer Matrix Method

To study light propagation in stratified media, once Maxwell's equations and the appropriate boundary conditions have been established, one of the best approaches is to calculate the Fresnel coefficients and use the complete refractive index of the system to consider absorption and its possible effects on polarization. An effective and well-known way to achieve this is to use the Transfer Matrix Method (TMM) [41]. This methodology also allows the calculation of the reflectance, density of states, and field intensity of different layers of the media. By correctly introducing a gain, possible emissions from the media can also be considered. This approach has already helped to study the influence of microcavities' asymmetry on their transmittance properties and strong-field effects [37], as well as on the formation and interaction of polaritons in p-Si at room-temperature [38]. In this study, the TMM was used to simulate the photonic response of a coupled system consisting of an asymmetric cavity completed by a layer of perovskite quantum dots.

2.2 Strong coupling model

The interaction of light with matter can be described under some approximations by a Jaynes-Cummings Hamiltonian as $H_0 = \sum_k E_X(k)\, b_k^\dagger b_k + \sum_k E_C(k) a_k^\dagger a_k + \sum_k \tilde{g}\,(a_k^\dagger b_k + b_k^\dagger a_k)$, where E_X is the exciton energy, E_C is the photon energy in the cavity, $a^\dagger(a)$ and $b^\dagger(b)$ are the creation (annihilation) operators for the photon and exciton, respectively, and $\tilde{g}$ is the coupling term, which can be also designated as Rabi splitting. The first term represents the electronic states of matter for a generic two-level system, the second term corresponds to a structured radiation field, and the third term describes the interaction between the two systems [42]. In a weak-coupling situation, the interaction can be described by the photon excitation of an electron from the ground state to the excited state. When coupling becomes more important, the structured light field and specific optical transitions are adequately described by the above Hamiltonian with its creation and annihilation operators. High coupling coefficients are generally obtained by increasing the number of quantum emitters and reducing the volume of the optical confinement modes [43].

In this work, we are using a simpler and more intuitive non-Hermitian Hamiltonian for coupled oscillators, which can be written as:

$$H = \begin{pmatrix} \omega_{cav} - i\frac{\gamma_{cav}}{2} & \tilde{g} \\ \tilde{g} & \omega_{ex} - i\frac{\gamma_{ex}}{2} \end{pmatrix}, \tag{1}$$

with the corresponding eigenvalue problem and polaritonic eigenvalues:

$$\begin{pmatrix} \omega_{cav} - i\frac{\gamma_{cav}}{2} & \tilde{g} \\ \tilde{g} & \omega_{ex} - i\frac{\gamma_{ex}}{2} \end{pmatrix} \begin{pmatrix} C \\ X \end{pmatrix} = \omega_{\pm} \begin{pmatrix} C \\ X \end{pmatrix}, \tag{2}$$

$$\omega_{\pm} = \frac{\omega_{cav}+\omega_{ex}}{2} - \frac{i}{2}\left(\frac{\gamma_{cav}}{2} + \frac{\gamma_{ex}}{2}\right) \pm \sqrt{\tilde{g}^2 + \frac{1}{4}\left(\delta - i\left(\frac{\gamma_{cav}}{2} - \frac{\gamma_{ex}}{2}\right)\right)^2}, \tag{3}$$

where ω_{cav} and ω_{ex} are the uncoupled cavity mode and QD exciton angular frequencies, respectively; γ_{cav} and γ_{ex} are their corresponding damping rates; ω_+ and ω_- are the frequencies of the hybrid states, which usually are referred as the high- and low-polariton branches, respectively. $\tilde{g}$ is the coupling strength, which is treated as a complex number in this work so that we can address both usual and mixed coupling conditions, as it will be shown below. $\delta = \omega_{cav}(\theta) - \omega_{ex}$ is the angular or in-plane k-detuning between the cavity and QDs exciton energies, considering explicitly the angle-resolved cavity mode. C and X are the Hopfield coefficients representing the cavity mode and the exciton weighting coefficients for each hybrid state, respectively, where $|C|^2 + |X|^2 = 1$. The energy separation between the hybrid polariton bands at the anti-crossing, $\delta = 0$, defines mode splitting or Rabi splitting as follows:

$$\Omega = \sqrt{4\tilde{g}^2 - \left(\frac{\gamma_{cav}}{2} - \frac{\gamma_{ex}}{2}\right)^2}. \quad (4)$$

Apart from δ- or k-detuning, strong coupling is also regularly studied in terms of the energy difference among the cavity and the exciton at normal incidence, that is, the cavity-detuning $\Delta = (\omega_{cav}(\theta) - \omega_{ex})_{\theta=0}$, where three cases are possible: negative $(\omega_{cav}(\theta) - \omega_{ex})_{\theta=0} < 0$, positive $(\omega_{cav}(\theta) - \omega_{ex})_{\theta=0} > 0$, or zero $(\omega_{cav}(\theta) - \omega_{ex})_{\theta=0} = 0$ detuning.

Note that this Hamiltonian is not diagonalizable at the critical coupling strength, given by $g_{EP} = |\gamma_{cav} - \gamma_{ex}|/4$, where the exceptional point of this coupled system gives rise to a Rabi splitting. Furthermore, as established in [22], for a two-level system in a Fabry-Perot-type microcavity, this approach allows the phenomenon of strong coupling to be treated both classically and quantum-mechanically.

To discuss the obtained results in terms of BICs and EPs, two considerations must be made. The first concerns the conditions required for non-vanishing Rabi splitting and spectrally separable resonances, given by $2|\tilde{g}| > \left|\frac{\gamma_{cav}}{2} - \frac{\gamma_{ex}}{2}\right|$ and $\Omega > \frac{\gamma_{cav}}{2} + \frac{\gamma_{ex}}{2}$, respectively [44]. The second is the condition for the occurrence of an EP, that is, when the square-root term in Eq. (3) is zero because the two eigenvalues coalesce [21]. As mentioned above, Rabi splitting occurs from this EP when a real coupling constant is assumed. However, for inversion population conditions, the non-Hermitian character of the system grants the coupling constant to be imaginary, and then the presence of mixed polaritonic states, even in the absence of damping [22], which will be verified for our system when considering its topological aspects.

2.3 Perovskite QDs fabrication

Regarding the perovskite QDs preparation, by following a typical hot-injection synthesis, 0.2 mmol of $PbBr_2$ (73.4 mg) and 5 mL of 1-octadecene were loaded in a 25 mL three-neck round bottom flask, the mixture was nitrogen purged at 120 °C for 1 hour, then 0.5 mL of oleylamine and 0.5 mL of oleic acid were injected into the reaction flask, the mixture was stirred until all $PbBr_2$ was completely dissolved. Then 0.2 mL of OLA-HBr at 80 °C and 0.5 mL of Cs-oleate at 100 °C were injected successively. The reaction mixture was cooled in an ice bath immediately after the final injection. Then, 5 mL of the crude solution was loaded into a centrifuge tube containing 5 mL of acetone and centrifugated at 7000 rpm for 30 min. After centrifugation, the supernatant was discarded, and the precipitate was dispersed in toluene. In this way, $CsPbBr_3$ QDs approximately 8-10 nm in size can be obtained (the corresponding micrograph is shown in the supplementary information, Fig. S1) [45].

2.4 p-Si cavities fabrication, complex refractive index calculation and photoluminescence measurement setup

Porous silicon (p-Si) microcavities were fabricated by electrochemical etching of p-type boron-doped crystalline silicon (c-Si) wafers with a (100) orientation and an electrical resistivity < 0.005 Ω cm. Before the etching process, an aluminum layer was evaporated on the backside of the c-Si wafers and heated to 550 ºC in an inert atmosphere for 15 min, to create an electrical contact. The Teflon cell was filled with an electrolyte composed of aqueous hydrofluoric acid (HF), ethanol, and glycerin at a volume ratio of 3:7:1. Electrochemical etching, in which the c-Si substrate acted as the cathode and a platinum mesh as the anode, was initiated by applying a constant electrical current. The porosity and thickness of the p-Si layer depend on the current density and etching time, respectively, both of which are computer-controlled using a Keithley 2450 Source Meter SMU Series. This control of the porosity and thickness determines the optical path length of each layer, allowing the tuning of its photonic response. To minimize the porosity gradient in each layer, pauses of 1 s every 4 s of etching were applied during the anodization. p-Si simple bilayers with low and high porosities were then fabricated by alternating the applied current density

during the electrochemical etching, between two values, 3 mA/cm^2 and 40 mA/cm^2, respectively, denoted as layers A and B. Multiple layer stack samples, or microcavities, were obtained by combining low- and high-porosity layers in a Distributed Bragg Reflector (DBR) sequence, where the conditions for the respective thicknesses, d_A and d_B, define their corresponding refraction indexes: $d_A = \frac{\lambda_{DBR}}{4n_A}$, $d_B = \frac{\lambda_{DBR}}{4n_B}$. After anodization, the samples were rinsed with ethanol and dried under a nitrogen flow. Finally, the p-Si samples were passivated by thermal oxidation at 300 °C for 30 min. Previously, a layer of aluminum was removed from the c-Si substrate to prevent its diffusion during thermal oxidation and to avoid possible Al contamination during the quantum dots deposition.

P-Si is a nano-structured material composed of a skeleton of c-Si surrounded by air. The complex refractive index, $\eta = n_R - in_I$, can be calculated using the effective medium approximation (EMA), following Estrada-Wise and del Río [46], as shown in [38].

Angle-resolved photoluminescence (ARPL) was measured at the University Laboratory of Optics at Surfaces (Laboratorio Universitario de Óptica de Superficies) into the Physics Institute of UNAM (LOS-UNAM). The sample was excited at 355 nm using an EKSPLA PL2231-50-SH/TH Nd:YAG pulsed laser System featuring ~26 ps pulses with a repetition rate of 10 Hz. The spot diameter was fixed at 3.6 mm by using a diaphragm. The emission of the sample was collected using an optical fiber (Ocean Optics model P1000-2-UV-VIS with a core of 1000 µm) and analyzed using an Ocean Optics USB2000+ UV-VIS spectrometer. Both the sample and optical fiber were attached to a rotational Newport RSP-1T plate to control the incidence and emission angles, respectively.

3. Results and discussion

3.1 qBICs and EPs

Recently, we discussed the presence of qBICs in asymmetric photonic crystals [37] and aperiodic quasi-crystals [38]. When considering intrinsic-lossy, non-Hermitian systems, such as p-Si, the introduction of an asymmetry can reduce reflectance of a given mode compared to the case of the symmetrical micro-cavity and enable an increase in the field strength within this novel cavity [37]. This result is directly related to the appearance of robust states, with practically zero bandwidth and large factor quality, giving rise to a broadband large Purcell factor, that is, the previously discussed qBICs [47-49]. In this study, we selected an asymmetric mirror cavity as the photonic component of the coupled system. This cavity, as shown in Fig. 1(a), consists of ten pairs of alternating layers with different refractive properties, A and B, with a defined thickness of each one, an extra layer of type A at the bottom to break the mirror cavity, and a layer called a defect of type B, whose thickness can be varied at the top. Fig. 1(a) shows the selected design, while Fig. 1(b) shows the reflectance at normal incidence (k = 0), and the corresponding density of states (DOS), which can be obtained for a given set of fabrication parameters, considering a non-zero cavity-detuning. Here, these parameters are set to maximize reflectance at the QDs' emission wavelength (around 510 nm). The importance of the fabrication parameters is discussed in detail in the next section when discussing mixed polaritons.

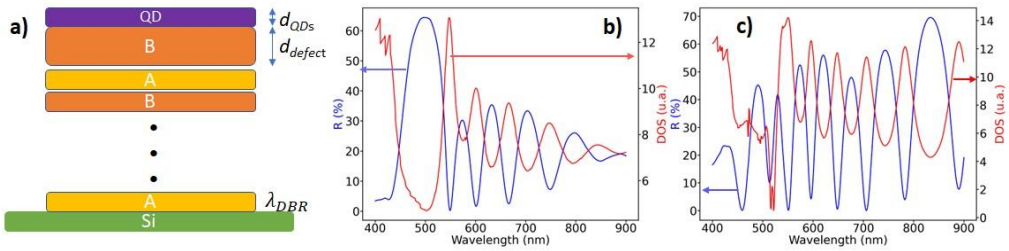

Fig. 1. (a) Asymmetric mirror cavity design, normal incidence reflectance (R%) and density of states (DOS) as a function of the wavelength (b) without and (c) with the perovskite quantum dot layer. These curves in (b) and (c) are obtained for film thicknesses $d_A = 66.97$ nm, $d_B = 95.85$ nm, $d_{defect} = 590$ nm, and $d_{QD} = 110$ nm for (c).

The coupled system was obtained by depositing a layer of perovskite QDs on top of the asymmetric mirror cavity, that is, on the top defect layer B. The thicknesses of the defect layer and the QD layer are adjustable parameters. The large density of states and the corresponding field localization (not shown in Fig. 1) are evidence of the BIC nature of the cavity modes that can be obtained for this design. Figure 1c) shows that the strong coupling between the perovskite quantum dots and the photons confined in the asymmetric cavity thus formed results in the appearance of new narrower and deeper reflectance modes. The emission peak of this pol-BIC mode (reflectance dip around $\lambda_{pol-BIC} = 523.9$ nm) gives a quality factor ($Q = {\lambda_{pol-BIC}}/{\gamma_{pol-BIC}}$=) of about 2.2×10^6. This Q-value is obtained by curve fitting using a Lorentzian function with a width at half maximum equal to $\gamma_{pol-BIC} = 0.24$ pm. As shown in the next section, the signature of qBICs is manifested by reflectance dips and divergence of emission at the corresponding energies and k-positions. This is a result of a large Purcell factor and a corresponding small decay rate associated with the BIC. However, there is another immediate consequence: the damping of this mode and the photoluminescence (PL) peak decrease to almost zero.

There are conditions where the coupling constant $\tilde{g}$ becomes imaginary: this occurs when $\gamma_{cav} = \gamma_{ex}$, and the cavity detuning is non-zero. These exceptional points, identified as EP2 in Ref. [22], may be associated with a population inversion condition where the polaritonic modes of the coupled system merge into a single mode. We will also see in the next section, that the dispersion relations giving rise to mixed polaritons can only be reproduced by considering a complex coupling constant.

Note that mixed polaritons, emerging from this kind of EPs, had already been predicted before, given that the energy spectrum is continuous [50], which is satisfied here, because the non-Hermitian Hamiltonian of Eq. (1) can be classified as a Hamiltonian of the von Neumann-Wigner type, characterized by a bounded potential [51]. These previous studies lead to conclude that the resulting mixed polaritons are also BICs, that is, BIC-polaritons, or pol-BICs as they are commonly referred to in the literature, which are the corresponding eigenfunctions of this type of EPs.

3.2 Mixed polaritons

Based on previous results [37,38], we have analyzed the influence of several structural parameters of the photonic cavity on their qBIC modes and on the polariton (pol-BIC) formation. In particular, we studied the effect of changing the defect and QD layer thicknesses d_{defect} and d_{QD}, as well as the value of λ_{DBR}, defined by the condition for the DBR sequence $n_A d_A = n_B d_B = {\lambda_{DBR}}/{4}$, for values not necessarily close to the exciton wavelength emission. The consequences of these variations on the light-matter interaction for this coupled system were studied by implementing a Python code based on the TMM, as mentioned previously.

Simulated angle-resolved reflectance spectra obtained for the asymmetric mirror cavity configuration shown in Fig. 1, are plotted in Fig. 2. The simulated spectra obtained without the QD layer are shown in Fig. 2(a) for $d_{defect} = 590$ nm and $\lambda_{DBR} = 480$ nm. The corresponding simulated spectra by considering a strong coupling with a 100 nm-thick perovskite QD layer are plotted in Fig. 2(b), between 2.1 and 2.6 eV, where the QD exciton resonance is expected. In Fig. 2(a), the presence of a deep reflectance dip at different energies, and around *k* momentum values of $\pm1\times10^7$ nm^{-1} (angular range ±40-60 °), can be the

signature of a qBIC resonance. The hybridization of optical cavity modes and QD excitons gives rise to pol-BICs. Fig. 2(b) shows that the dispersion relation (around 2.4 eV) exhibits two branches, characteristic of Lower- (LP) or Upper-polaritons (UP). For instance, LPs are more intense and exhibit a narrower energy dispersion.

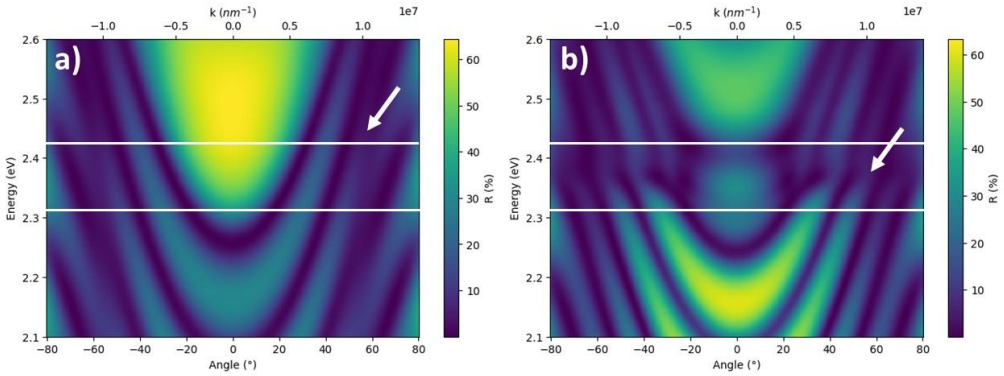

Fig. 2. Angle-resolved reflectance simulation results obtained for an asymmetric mirror cavity (a) without quantum dot layer, and (b) by considering a strong coupling with a perovskite quantum dot layer. White arrows mark the qBIC mode and the corresponding pol-BIC formed after the hybridization. White horizontal lines mark the 2.32 and 2.43 eV energies mentioned for Fig. 3(b).

Fig. 3(a) shows the experimental photoluminescence (PL) of perovskite QDs in solution and deposited on a p-Si membrane, while Fig. 3(b) shows the simulated characteristic emission from LP and UP pol-BICs at approximately 2.36 eV (526 nm) and 2.41 eV (515 nm), for an angle of 58.5°, respectively, in the case of a very small damping parameter $\gamma_{pol-BIC}$. For the QD/cavity coupled system considered here, the intensity contrast is visually much easier to identify (due to limitation in the signal to noise ratio) in the emission configuration than in the reflection configuration. In the rest of this work, we used angle-resolved photoluminescence results (simulations and measurements) to study pol-BIC formation.

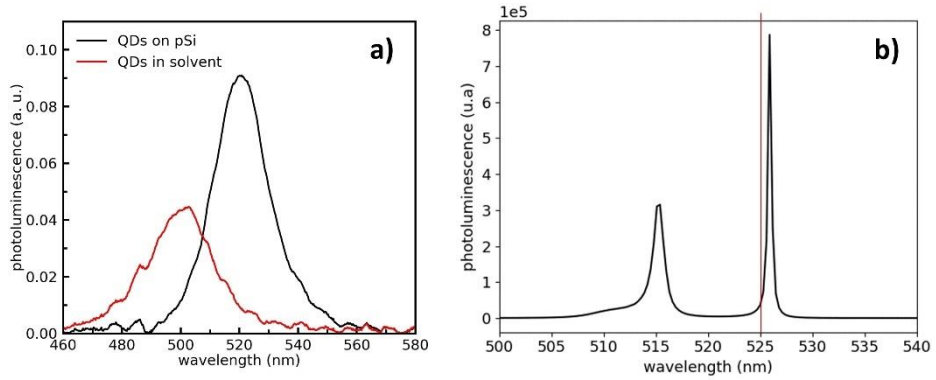

Fig. 3. Experimental emission from the perovskite QDs in (a) solution, on a p-Si layer, and (b) simulated emission at 2.36 eV (526 nm) and 2.41 eV (515 nm) from LP and UP pol-BICs, respectively. The vertical red line separates the two regions corresponding to the UP [500, 525] and LP [525, 540], respectively.

The specific character of the various types of pol-BICs, including mixed polaritons associated with certain exceptional points where the coupling constant becomes imaginary,

should manifest itself in their dispersion relation. In this work, we sought to identify a set of parameters for which strong emission peaks from our QD/cavity coupled system can be ascribed to BIC resonances. Figures 4(a)-(d) present the simulation results of the peak PL intensity emitted by the coupled system, for a range of values for d_{defect} and d_{QD}, regardless of the wavevector value, in two wavelength regions, [500, 525] and [525, 540], corresponding to the UP and LP, respectively (separated in Fig. 3 by the vertical red line). Note that 525 nm (2.36 eV) is the wavelength emission of the isolated $CsPbBr_3$ perovskite QDs. Figures 4(a) and 4(b) show the UP emission with and without considering absorption from the p-Si and perovskite systems, respectively, whereas Figures 4(c) and 4(d) show in an analogous way the LP emission. To illustrate how values of these maps are obtained, that is, how the peak intensity emitted by the coupled system is obtained, for both UP and LP, with and without absorption, Figures 4(e) and 4(f) show simulated emission spectra at some discrete angles, and for a pair of d_{defect} and d_{QD} values, corresponding to the marked points 1 and 2 in Fig. 4(a), respectively. For point 1 ($d_{defect} = 220\ nm, d_{QD} = 250\ nm$), the peak PL intensity for the UP emission corresponds to that measured at -72° (red spectrum in Fig. 4(e)), while for point 2 ($d_{defect} = 220\ nm, d_{QD} = 10\ nm$), it corresponds to the UP emission measured at -69° (red spectrum in Fig. 4(f)). These maps show parameter regions where pol-BICs are more likely to emerge. In particular, for thick QD layers (> 280 nm), regions of high PL intensity are less prominent when the imaginary part of the QD layer's refractive index is not considered (no QD absorption). Although counter-intuitive, this is a manifestation of the qBIC mode, for which interference between different radiative dissipation modes is destructive. For smaller QD layer thicknesses (< 200 nm), the effect of taking QD absorption into account on the PL intensity of LPs and UPs is more subtle, and we will come back to these considerations in the next paragraph. However, considering the patterns formed for both UP and LP emissions, there seems to be a shift when considering the absorption. To analyze this, attention should be focused on the region of 0-100 nm for d_{QD}, varying d_{defect}, for the UP, with and without absorption, that is, the left side of Figs. 4(a) and 4(b), respectively. From these figures, a periodicity of approximately 215 nm was established. By considering the refractive index of the defect layer, this periodicity becomes $L_{per} = n_B * L \approx 1.22 * 215 \approx 260.2\ nm \approx \frac{525}{2} \rightarrow \frac{\lambda_{exciton}}{2}$.

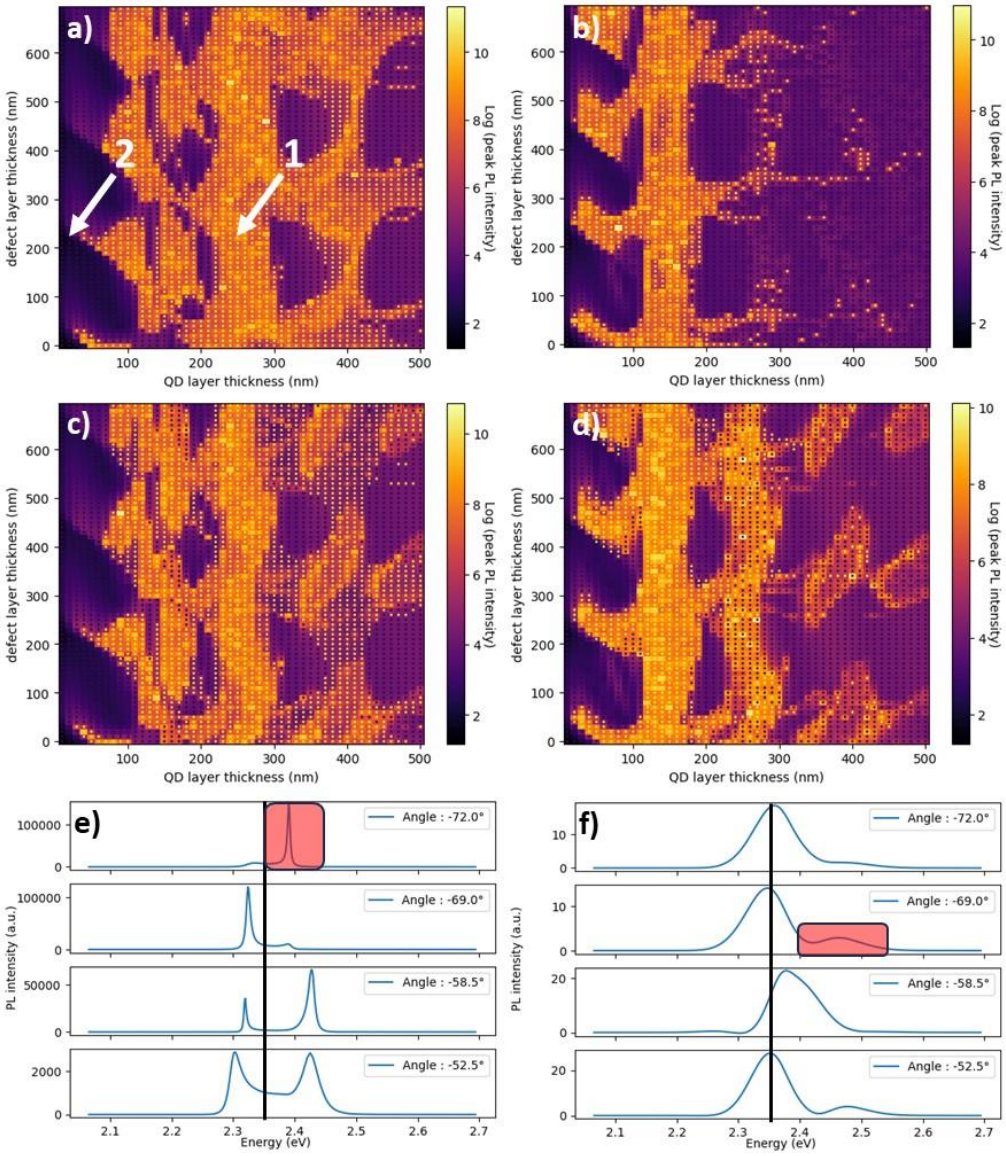

Fig. 4. Simulation results showing the cartography of the peak PL intensity of the QD/cavity coupled system when varying d_{defect} and d_{QD}. (a) UP with absorption, (b) UP without absorption, (c) LP with absorption, and (d) LP without absorption. (e) and (f) Simulated emission spectra for some wavevectors from points 1 and 2 in part (a), respectively. Black vertical line marks the exciton emission from isolated QDs. The red squares in (e) and (f) indicate spectral regions where the intensity of the UP peak is maximal.

To identify the set of parameters of the QD/cavity structure for which pol-BICs will emerge from the presence of a qBIC, we have performed a parametric analysis where the angle-resolved PL spectra were obtained for different thicknesses of the QDs layer (d_{QD}) and the photonic cavity condition (λ_{DBR}), for a fixed defect layer thickness (d_{defect}). The presence of pol-BICs manifests itself by a very high PL intensity (here arbitrarily considered larger than 10^5). Figure 5 shows the simulation results obtained for $\lambda_{DBR} = 500$ nm. For this set of parameters, UPs emerge at minimum reflectance values (Fig. 5(a)), while LPs appear at maximum reflectance values (Fig. 5(b)). This directly corresponds to the results shown in Fig.

4: because absorption minimizes reflectance, UPs are more intense when absorption is considered (Fig. 4(a)), whereas LPs are more intense when there is no absorption, that is, when the reflectance is higher, as shown in Fig. 4(d). A second observation obtained from this parametric analysis is the coexistence of several UPs and/or LPs that are likely to be separated by a resonance reflectance dip, as shown in Fig. 5(c), because several exist for certain cavity parameters, as shown in Fig. 1.

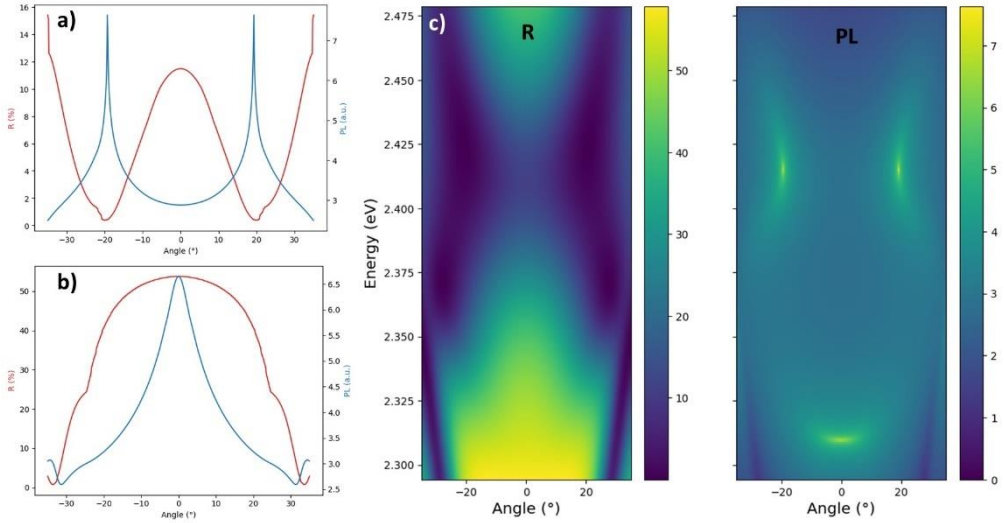

Fig. 5. (a) UP and (b) LP reflectance (the red curve corresponds to the left scale) and photoluminescence intensity (the blue curve corresponds to the right scale) from pol-BICs. (c) Angle-resolved pol-BIC reflectance and PL intensity obtained for $d_{QD} = 104$ nm, with $\lambda_{DBR} = 500\ nm$ and fixed $d_{defect} = 590\ nm$.

The dispersion relation for the cavity mode can be described in terms of the angular position (wavevector k) as $\omega_{cav}(\theta) = \omega_{cav}(0)\left(1 - \frac{sin^2(\theta)}{n_{eff}^2}\right)^{-\frac{1}{2}}$, where $\omega_{cav}(0) = \omega_0$ is the cavity mode energy at normal incidence and n_{eff} is the cavity effective refraction index. The value of $n_{eff}(\lambda)$ can be approximated by the refractive index of the defect layer, assuming that the incident electric field is maximal in this layer and considering conditions where $d_{defect} >> d_{QD}$. Our simulations also show that the cavity mode frequencies are essentially determined by the characteristic λ_{DBR} value of the periodic structure ($\omega_0(\lambda_{DBR}, d_{defect}, d_{QD}) \approx \omega_0(\lambda_{DBR}, d_{defect}) = \omega_o(\lambda_{DBR})$), with a variation quite small around the bandgap of the perovskite system considered in this study (2.4 eV). Finally, the dispersion relation for pol-BICs is obtained using Eq. (3) with $\gamma_{cav}, \gamma_{ex} \to 0$. In the following, we have set the value of d_{defect} to 590 nm and sought to reproduce the dispersion relations of pol-BICs by varying n_{eff} and the exciton/photon coupling strength ($\tilde{g}$). For d_{QD} values between 90 and 110 nm, the dispersion relations have been reproduced using a parameterization for the n_{eff} and $\tilde{g}$ quantities. The effective refractive index of the cavity is written as a Cauchy relation of the form $n_{eff}(\lambda) = A + B/\lambda^2$, while $\tilde{g}$ is considered to vary linearly with the thickness of the QD layer, i.e. $\tilde{g} = Cd_{QD} + D$. For most of the map areas in figures 4(a) and 4(c), showing pol-BICs, with peak intensities greater than 10^5, the best curve fits for their dispersion relations are obtained for the following set of parameters for the hybrid cavity: $A = 1.192$; $B = 14\,000\ nm^2$; $C = 1.4 \times 10^{-3}\ m^{-1}s^{-1/2}$; $D = -0.0785\ s^{-1/2}$. However, there are other specific map points in Fig. 4, where pol-BICs dispersion relations can only be reproduced for an imaginary coupling strength. From the

strong coupling model given above, we noted earlier the existence of a critical coupling strength, where an EP occurs when the square-root term in Eq. (3) is zero, and Rabi splitting is manifested. In the absence of BICs, this condition is given by $g_{QEP} = |\gamma_{cav} - \gamma_{ex}|/4$, considering zero *k*-detuning. However, when a qBIC is present and a pol-BIC is formed, then $\gamma_{cav}, \gamma_{ex} \to 0$, and the previous condition for strong coupling is now given by $g_{QEP} = (\omega_{cav}(\theta = 0) - \omega_{ex})/2$. For this condition, the emission intensity is divergent, which can be considered as a population inversion condition, for a system with a non-zero cavity-detuning. Therefore, the condition becomes $\tilde{g}^2 + \delta^2/4 = \tilde{g}^2 + (\omega_{cav}(\theta) - \omega_{ex})^2/4 = 0$. The EPs that give rise to this specific coupling condition are those identified as EP2 in Ref. [22] and the corresponding coupling constant becomes imaginary:

$$\tilde{g} = i\delta/2. \quad (5)$$

In the supplementary information, Fig. S2 presents GIF images showing the evolution of the pol-BIC dispersion relation for real and imaginary $\tilde{g}$ values, for both positive (top plot) and negative (bottom plot) non-zero cavity-detuning at normal incidence. Dispersion relations of normal polaritons, for which the UP and LP branches lie outside the QD exciton and the photonic cavity energy limits, are obtained when $\tilde{g}$ is pure real. For pure imaginary $\tilde{g}$ values, exotic dispersion relations, associated with mixed polaritons, can present a distinctive C-shape where the upper and lower polariton characters merge at an exceptional point of the second type (EP2: see discussion above), besides of a polariton superposition.

Figure 6 shows a series of angle-resolved PL simulation results obtained for d_{defect} = 590 nm, λ_{DBR} = 480 nm, and for a QD layer thickness (d_{QD}) varying from 92 nm to 112 nm. Positive cavity-detuning values are considered for these simulations. As mentioned previously, pol-BIC dispersion relations are obtained using Eq. (3), considering pure imaginary $\tilde{g}$ values. The values of the norm of $\tilde{g}$, corresponding to the different graphs in Fig. 6, are given in Table 1. For these graphs, note that polariton energies are always contained within the QD exciton and photon cavity energy limits (in direct agreement with the GIFs images). As d_{QD} increases, $|\tilde{g}|$ increases and the mixing of the polaritons is made more evident, passing from two separated LP and UP polaritons ($d_{QD} = 92$ nm), to a polariton superposition ($d_{QD} = 96, 100, 104$ and 108 nm), to more exotic dispersion relations showing two or several exceptional emission points ($d_{QD} = 112$ nm), indicating topological aspects that will be discussed into the next section. There is indeed a continuous spectrum of emissive states, resolved in angle, between the exceptional points, which reflects the presence of superposition of polaritonic states, even though the intensity of these states decreases as the separation between the exceptional points increases. We would like to emphasize that this set of mixed states, whose presence correlates with the appearance of EP2-type exceptional points, reflects a break in parity-time symmetry (PT-symmetry), i.e. a transition from a symmetrical phase to a symmetry-breaking phase [52-54]. In other words, we pass from a system in equilibrium to a system in nonequilibrium, although the non-Hermitian system is always in dynamic equilibrium and energy is conserved, causing the energy to acquire an imaginary component. This is shown in Figure 7, in the transition from gray to white regions. This PT-symmetry phase transition clearly indicates the non-Hermiticity of our system, and therefore its control flexibility through the tuning of its parameters [53,54]. All these exotic dispersion relations result from the hybridization of the pol-BICs: we call them mixed polaritons, showing an imaginary coupling constant, as given by Eq. (5). In the supplementary information, we have drawn a map (see Fig. S3) to delimit the zones in the parameter space of our hybrid cavity, for which normal polaritons (yellow zones) and mixed polaritons (red zones) are observable. Note that the mixed polaritons occurs at periodic regions defined by $\lambda_{DBR}/2$ integral periods.

The hybridizing scheme for real and for imaginary $\tilde{g}$ (polariton energies either external or contained within the QD exciton and photon cavity energy limits) represent a complete set of dressed states, that is, the stationary response of a two-level system to an optical field [55,56].

An additional advantage of considering the full extent of strong coupling, by admitting real and imaginary coupling constants, is the possibility of observing a Mollow triplet [57], that is, a triple emission line from a two-level system under the influence of an optical field, as is shown in Fig. 6 when considering $d_{QD} = 112\ nm$: several emission peaks can be observed at an angle of approximately 24°. This feature could be very relevant for applications in quantum technology.

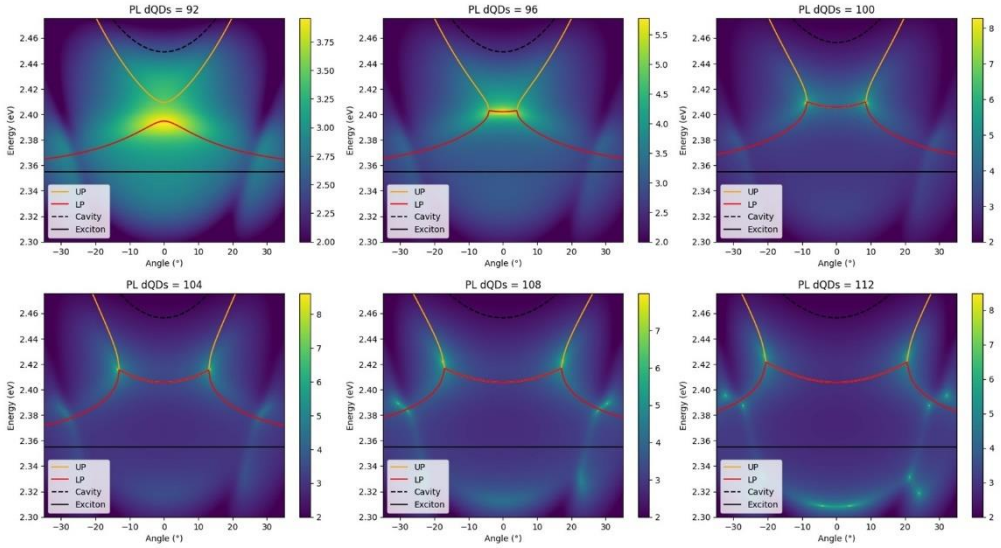

Fig. 6. Simulation results of the angle-resolved PL intensity in logarithmic scale and the corresponding dispersion relations of mixed polaritons for different QD layer thicknesses (d_{QD}), with $\lambda_{DBR} = 480\ nm$ and fixed $d_{defect} = 590\ nm$.

Table 1. Coupling constant for mixed polaritons.

$\mathbf{d_{QD}}$ **(nm)**	$\widetilde{\boldsymbol{g}}$ **(meV)**
96	45
100	48
104	51
108	54
112	59

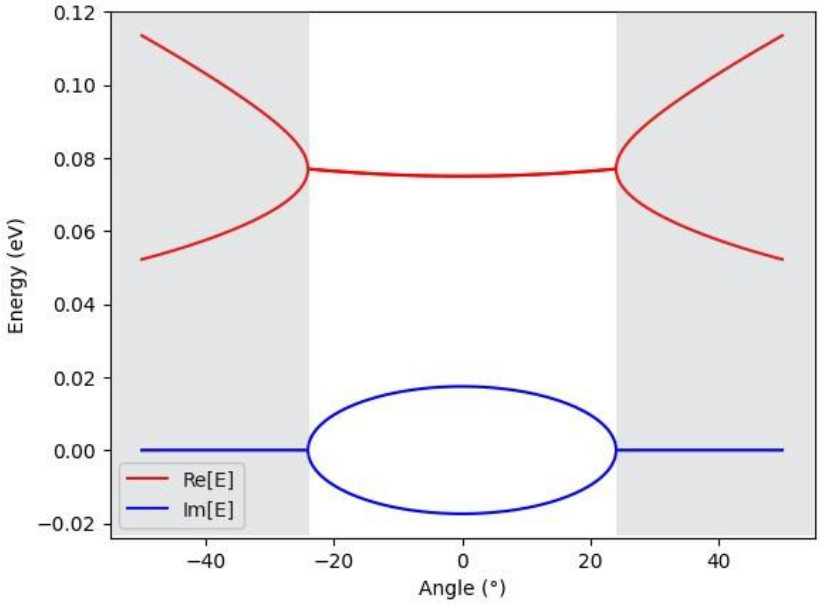

Fig. 7. PT-symmetry phase transition from the symmetric (grey regions) to the symmetry-broken (white region) phase, where eigenenergies become complex ($\tilde{g} = i0.077$ eV) when crossing EP2-type exceptional points.

3.3 Topological aspects of mixed polaritons

To better understand the merging of the polaritonic modes, that is, a population inversion condition indicating the presence of EP2-type exceptional points, and therefore the expression of complex coupling constants, it is helpful analyzing the topological nature of mixed polaritons. As indicated in [31], pol-BICs have a topological nature inherited from qBICs, which are at the origin of their formation, even though these qBICs have a finite quality factor. For 1D photonic systems, their topological aspects are characterized by the Zak phase [58], which can be calculated according to the surface bulk correspondence as $\exp\left(i\theta_n^{\mathrm{Zak}}\right) = -\frac{\mathrm{sgn}(\phi_n)}{\mathrm{sgn}(\phi_{n-1})}$, which can have values of 0 or π, and ϕ_n, ϕ_{n-1} are the reflection phases in the bandgaps above and below the n_{th} electronic band [38]. To calculate the Zak phase for our system, first, because the cavity is not a symmetrical structure, the electronic band structure was calculated by considering all the sequence as the unit cell. Because the actual system is composed of only one unit cell, a layer of air among the unit cells was also considered in the calculation, with a thickness of 1 μm. From the reflectance and reflection phases calculated under this assumption, as shown in Fig. 8(a) for a qBIC, it is evident that there is a discontinuity in the Zak phase, which introduces an interface state in the gap between the electronic bands where this discontinuity occurs, also indicating electronic band inversion, that is, exchange of the conduction and valence bands after band crossing, which is a topological transition [38,58,59]. The gap where the discontinuity is observed, that is, the change from 0 to π, is centered at 2.4 eV, that is, the gap tuned to the exciton of the perovskite QDs. The discontinuity in the Zak phase has been recognized as a signature of the existence of a topological mode, which is evidenced by the rigorous relationship between the Zak phase and reflection phase given by the previous equation and its corresponding numerical or experimental verification [58]. The analysis was preserved when the coupled system was considered, as shown in Fig. 8(b). It is worth noting that the discontinuity is not perfect because we are dealing with imperfect BICs, that is, qBICs. Nevertheless, this topological transition, given by electronic band inversion, marks the appearance of exceptional points when the Zak phase is zero in its transition from the positive to negative values of the

reflection phase, that is, at the interface state in the gap. Therefore, this topological nature of mixed polaritons reinforces the modeling of their dispersion relation using imaginary coupling coefficients.

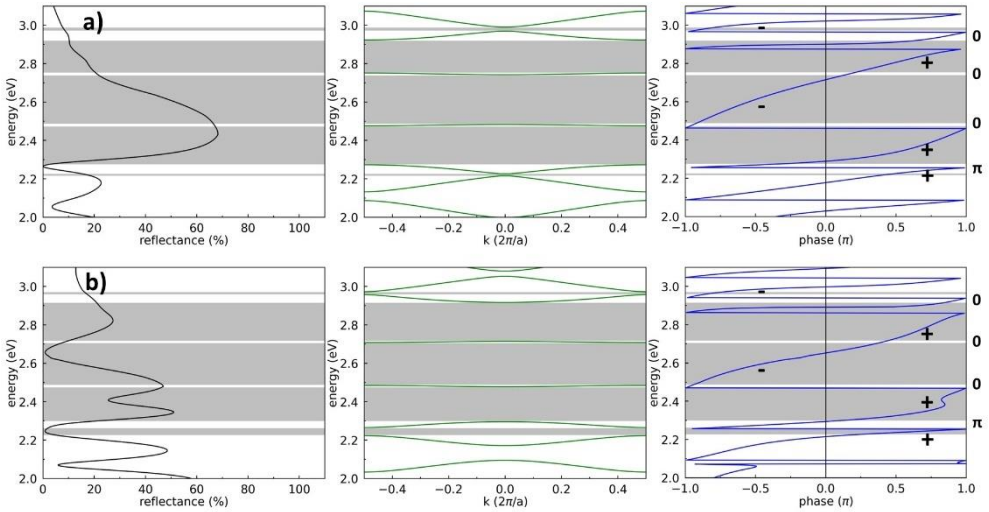

Fig. 8. From left to right, reflectance, band structure and reflection phase for (a) the asymmetric cavity and (b) the coupled system. Zak phase discontinuity is illustrated in the reflection phase for both cases.

3.4 Experimental results

From the polariton classification shown in Fig. S3, in the supplementary information, it turns out that the experimental demonstration of mixed polaritons requires precise sample fabrication. Otherwise, normal polaritons are obtained in the best case. Slight deviations from a given set of fabrication parameters, $(\lambda_{DBR}, d_{defect}, d_{QD})$, can result in mixing of different types of polaritons, making it difficult to correctly classify them. From our experience, we found that it is difficult to obtain the required thickness for the perovskite QD layer. Moreover, despite great efforts, the obtained deposits are not homogeneous in terms of thickness and QD density, which has, as an additional consequence, a variation in the refractive index that could be sufficient to hide mixed polaritons. An example of the inhomogeneity of the thickness, which implies changes rather abrupt, can be seen in Fig. S4. On the other hand, the variation in the QD density was mainly due to the use of ligands. In contrast, the p-Si cavity parameters were robust enough to preserve strong coupling, as observed here and in our previous results [38], although eventual oxidation, even if minor, of the cavity structure could alter the refractive index sufficiently to complicate the visualization of mixed polaritons. Therefore, experimental evidence for mixed polaritons is still in progress, and the experimental results presented below show their first glimpse.

A sample with parameters $(\lambda_{DBR} = 480\,nm, d_{defect} = 590\,nm, d_{QD} = 50\,nm)$ was fabricated. First, electron microscopy experimental conditions were found to provoke the evaporation of some parts of the perovskite QD thin film deposited on the p-Si cavity surface. From the resulting islands, a thickness of 50 nm was measured and used in the corresponding simulations (see corresponding images in the supplementary information, Fig. S4). Because our ARPL setup is based on emission acquisition using an optical fiber, instead of the typical Fourier-Transform one using a microscope objective, the numerical aperture of the fiber naturally increases the wavevector or angular data dispersion, explaining the diffuse shape of the normalized emission shown on the right side of Fig. 9(b). It is also worth noting that the ARPL measurements clearly show a shift of more than 30 nm in the emission peak, providing

evidence of polariton formation, as no shift was observed for the perovskite QD solution or for the perovskite QD deposited on a single p-Si monolayer when varying the angular position of the optical fiber (see Fig. S5). Consequently, the dispersion relations to fit the simulated and experimental normalized data shown in Fig. 9(b) must consider a non-zero coupling, either real or imaginary. A set of three pairs of polaritons can be used to fit the simulated and experimental data (see Fig. S6), with one pair always being a normal polariton and a real coupling corresponding to a Rabi splitting of 28 meV (extreme left signal in the simulated data of part (b)). The other two pairs (central and extreme right in the simulated data of part (b)) can be fitted either using normal polaritons, with a real coupling corresponding to a Rabi splitting of 16 meV for both (Fig. S6(a)), or mixed polaritons, with an imaginary coupling corresponding to a negative Rabi splitting of -16 meV (Fig. S6(b)). As observed in Fig. 9(c) and (d), where a zoom of the central data of part (b) has been applied (region marked by the arrow), to our best judgement, mixed polaritons allow, in general, the best fitting of the simulated or measured emission. As previously mentioned, this work is still in progress, and strong evidence of mixed polaritons is being actively investigated.

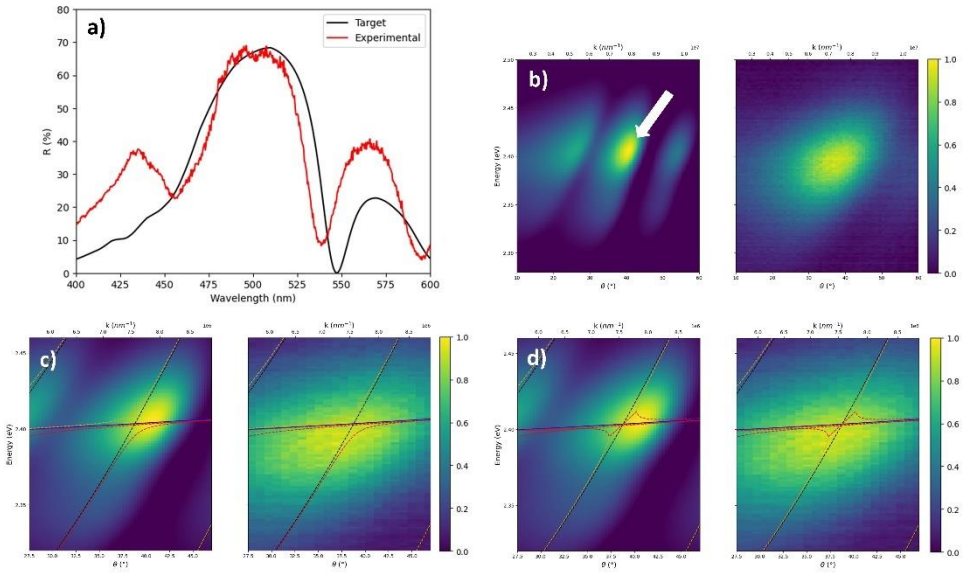

Fig. 9. Experimental results for M1 sample. (a) Reflectance at normal incidence. (b) ARPL best-fit simulation for $d_{QD} = 32$ nm (left) and measurement (right) for sample M1. Dispersion relationships using (c) normal (real g) and (d) mixed (imaginary g) polaritons. Blue dashed line represents the exciton dispersion, black dashed lines the cavity modes, and orange (red) dashed lines represent the upper (lower) polaritons.

4. Conclusions

In this study, using the physical properties of quasi–Bound States in the Continuum to provoke the manifestation of Exceptional Points of the appropriate type, we present numerical and experimental evidence of mixed polaritons, for which an imaginary coupling coefficient is necessary. From the numerical approach, an empirical parametrization relationship can be deduced, which is related to the strong coupling model. The non-Hermitian nature of the Hamiltonian used has enabled us to highlight the complex character of the corresponding coupling coefficient for mixed polaritons.

To support the appearance of the corresponding EPs giving place to the imaginary coupling coefficient, a topological transition was made evident using the Zak phase. This topological transition, caused by band inversion, occurs when the reflection phase changes from zero to π. This discontinuity introduces an interface state in the gap between the bands where it occurs, which in this case corresponds to that directly related to the exciton used to form polariton quasiparticles. Therefore, the topological nature of mixed polaritons reinforces the modeling of their dispersion relation using a complex coupling coefficient.

Finally, preliminary experimental evidence of these mixed polaritons was obtained at room-temperature for a $CsPbBr_3$ perovskite system using p-Si microcavities. The simplicity of the porous silicon photonic structure used to obtain these results is worth noting. The structure was fabricated without any special characteristic conditioning of reproducible strong coupling of the photonic cavity with this emissive system at room temperature. Despite its natural disorder and many structural defects on the nanometer scale, its topological features make it robust and stable for strong coupling with quantum emitters in a systematic manner. The main parameter to be carefully controlled during the fabrication process being the thickness of the perovskite QDs layer. Thus, there is room for improvement in the porosity of these photonic structures, their interactions with excitonic systems, and the resulting strong coupling between them.

Funding. ECOS-Nord CONACyT-ANUIES 315658; National Science Foundation (456789); PAPIIT-UNAM IN112022. PASPA-UNAM.

Acknowledgments. This research was partially funded by the ECOS-Nord CONAHCyT-ANUIES 315658, PAPIIT-UNAM IN112022, and PAPIIT-UNAM IN109122. J.A.R.E. is grateful for the sabbatical funding from PASPA-DGAPA-UNAM, CONAHCyT, and the University of Sherbrooke. S.E.G. thanks CONAHCyT for postdoctoral fellowship. V. F. thanks MITACS scholarship. The authors wish to acknowledge the technical assistance provided by Gerardo Daniel Rayo López and Gabriel Laliberté; Rogelio Morán Elvira, José Campos Álvarez and Carlos Magaña Zavala with the SEM images. LN2 is an International Research Laboratory (IRL 3463) funded and co-operated in Canada by Université de Sherbrooke (UdS) and in France by Centre National de la Recherche Scientifique (CNRS), as well as by Ecole Centrale Lyon (ECL), Institut National des Sciences Appliquées de Lyon (INSA Lyon), and Université Grenoble Alpes (UGA). It is also supported by the Fonds de Recherche du Québec Nature et Technologies (FRQNT). The work was also financially supported by CMC Microsystems.

Disclosures. The authors declare no conflicts of interest.

Data availability. The data underlying the results presented in this study are available upon reasonable request.

Supplemental document. See Supplement 1 for supporting content.

References

1. J. J. Hopfield, "Theory of the Contribution of Excitons to the Complex Dielectric Constant of Crystals," Physical Review **112** (5), 1555-1567 (1958). doi: 10.1103/physrev.112.1555.
2. Editorial, Polariton Plurality, Nature Mater. **21**, 721 (2022). doi: 10.1038/s41563-022-01313-2.
3. T. Byrnes, N. Kim, and Y. Yamamoto, "Exciton–polariton condensates," Nature Phys. **10**, 803–813 (2014). doi: 10.1038/nphys3143.
4. S. J. Won et al., Polariton lasing of multiple-layered InGaN/GaN/AlGaN axial heterostructure nanorods for tunable nanolasers. ACS Photonics 9, 3234-3244 (2022). doi: 10.1021/acsphotonics.2c00251.
5. E. Togan, Y. Li, S. Faelt, W. Wegscheider, and A. Imamoglu, "Polariton electric-field sensor," Phys. Rev. Lett. **125**, 067402 (2020). doi: 10.1103/PhysRevLett.125.067402.
6. M. C. Anderson, E. J. woods, T. P. Fay, D. J. Wales, and D. T. Limmer, "On the mechanism of polaritonic rate suppression from quantum transition paths," J. Phys. Chem. Lett. 14 (30), 6888-6894 (2023). doi: 10.1021/acs.jpclett.3c01188.
7. S. Ghosh, T. C. H. Liew, "Quantum computing with exciton-polariton condensates," npj Quantum Information **6**, 16 (2020). doi: 10.1038/s41534-020-0244-x.
8. C. Nayak, S. H. Simon, A. Stern, M. Freedman, S. Das Sarma, Non-Abelian anyons and topological quantum computation. Rev. Mod. Phys. 80, 1083–1159 (2008). doi: 10.1103/RevModPhys.80.1083.
9. C. W. Hsu, B. Zhen, J. Lee, S. L. Chua, S. G. Johnson, J. D. Joannopoulos, and M. Soljacic, "Observation of trapped light within the radiation continuum," Nature **499**, 188-191 (2013). doi: 10.1038/nature12289.
10. C. Hsu, B. Zhen, A. Stone et al., "Bound states in the continuum," Nat Rev Mater **1**, 16048 (2016). doi:10.1038/natrevmats.2016.48
11. D. C. Marinica and A. G. Borisov. Bound state in the continuum in photonics, Phys. Rev. Lett. 100, 183902 (2008). doi: 10.1103/PhysRevLett.100.183902

12. G. Xu, H. Xing, Z. Xue, D. Lu, J. Fan, J. Fan, P. P. Shum, and. L. Cong, “Recent advances and perspective of photonic bound states in the continuum,” Ultrafast Sci. **3**, 0033 (2023). doi: 10.34133/ultrafastscience.0033.
13. K. Koshelev, A. Bogdanov, and Y. Kivshar, “Engineering with bound states in the continuum,” Opt. Photonics News **31**(1), 38-45 (2020). doi: 1047-6938/20/01/38/8.
14. L. Cong, R. Singh, “Symmetry-protected dual bound states in the continuum in metamaterials,” Adv. Opt. Mater. **7**(13), 1900383 (2019). doi: 10.1002/adom.201900383.
15. K. Koshelev, S. Lepeshov, M. Liu, A. Bogdanov, and Y. Kivshar, “Asymmetric metasurfaces with high-Q resonances governed by bound states in the continuum,” Phys. Rev. Lett. **121**(19), 193903 (2018). doi: 10.1103/PhysRevLett.121.193903.
16. C. Zhou, L. Huang, R. Jin, L. Xu, G. Li, M. Rahmani, X. Chen, W. Lu, and A. E. Miroshnichenko, “Bound States in the Continuum in Asymmetric Dielectric Metasurfaces,” Laser Photonics Rev **17**, 2200564 (2023). doi:10.1002/lpor.202200564.
17. S. Xie, J. Wang, W. Shen, C. Bai, S. Sun, and X. Guan, “Multiple bound states in the continuum based on the dielectric metasurface,” JOSA B **40**(8), 2129-2138 (2023). doi: 10.1364/JOSAB.495141.
18. C. M. Bender, S. Boettcher, “Real spectra in non-Hermitian Hamiltonians having PT symmetry,” Phys. Rev. Lett. **80**, 5243-5246 (1998). doi: 10.1103/PhysRevLett.80.5243.
19. W. D. Heiss, “Exceptional points of non-Hermitian operators,” J. Phys. A 37, 2455-2464 (2004). doi: 10.1088/0305-4470/37/6/034.
20. W. Gao, X. Li, M. Bamba, and J. Kono, “Continuous transition between weak and ultrastrong coupling through exceptional points in carbon nanotube microcavity exciton-polaritons,” Nat. Photonics 12, 362-367 (2018). doi: 10.1038/s41566-018-0157-9.
21. M.A. Miri, A. Alù, “Exceptional points in optics and photonics,” Science **363**(6422), eaar7709 (2019). doi: 10.1126/science.aar7709.
22. J. B. Khurgin, “Exceptional points in polaritonic cavities and subthreshold Fabry-Perot lasers,” Optica **7**(8), 1015-1023 (2020). doi: 10.1364/OPTICA.397378.
23. A. Fakharuddin, M . K. Gangishetty, M. Abdi-Jalebi, S-H. Chin, A. R. bin Mohd Yusoff, D. N. Congreve, W. Tress, F. Deschler, M. Vasilopoulou, and H. J. Bolink, “Perovskite light-emitting diodes,” Nat. Electron. **5**, 203-216 (2022). doi: 10.1038/s41928-022-00745-7.
24. C. Zhu, M. Marczak, L. Feld, S. C. Boehme, C. Bernasconi, A. Moskalenko, I. Cherniukh, D. Dirin, M. I. Bodnarchuk, M. V. Moskalenko, et al. “Room-temperature, highly pure single-photon sources from all-inorganic lead halide perovskite quantum dots,” Nano Lett. **22**, 3751-3760 (2022). doi: 10.1021/acs.nanolett.2c00756.
25. A. Swarnkar, A. R. Marshall, E. M. Sanehira, B. D. Chernomordik, D. T. Moore, J. A. Christians, T. Chakrabarti, and J. M. Luther, “Quantum dot-induced phase stabilization of α-$CsPbI_3$ perovskite for high-efficiency photovoltaics,” Science **354**, 92-95 (2016). doi: 10.1126/science.aag2700.
26. S. Cheng, Z. Qiao, Z. Wang, L. Xiao, S. Das, Y. T. Thung, Z. Yuan, V. D. Ta, W. Fan, Y-C. Chen, and H. Sun, “Single mode lasing from $CsPbBr_3$ microcrystals fabricated by solid state space-confined growth,” Adv. Optical Mater. **11**(15), 2203133 (2023). doi: 10.1002/adom.202203133.
27. S. Paul, G. Kishore, and A. Samanta, “Photoluminescence blinking of quantum confined $CsPbBr_3$ perovskite nanocrystals influence of size,” J. Phys. Chem. C **127**, 10207-10214 (2023). doi: 10.1021/acs.jpcc.3c01336.
28. M.-Ch. Yen, et al. “Tamm-plasmon exciton-polaritons in single-monolayered $CsPbBr_3$ quantum dots at room temperature,” Adv. Optical Mater. **11**, 2202326 (2023). doi: 10.1002/adom.202202326.
29. Ch-Ch. Liu, H-H. Hsiao, and Y-Ch. Chang, “Nonlinear two-photon pumped vortex lasing based on quasi-bound states in the continuum from perovskite metasurface,” Sci. Adv. **9**, eadf6649 (2023). doi: 10.1126/sciadv.adf6649.
30. I. A. M. Ibrahim, K. As’Ham, L. Huang, A. E. Miroshnichenko, W. Lei, and H. T. Hattori, “Strong coupling of exciton and high-Q mode in all-perovskite metasurfaces,” Adv. Optical Mater. **10**, 2101120 (2022). doi: 10.1002/adom.202101120.
31. N. H. M. Dang, S. Zanotti, E. Drouard, C. Chevalier, G. Trippé-allard, M. Amara, E. Deleporte, V. Ardizzone, D. Sanvitto, L. C. Andreani, C. Seassal, D. Gerace, and H. S. Nguyen, “Realization of polaritonic topological charge at room temperature using polariton bound states in the continuum from perovkite metasurface,” Adv. Optical Mater. **10**, 2102386 (2022). doi: 10.1002/adom.202102386.
32. L. Canham editor, “Handbook of Porous Silicon,” Second Edition. Springer Cham, Switzerland (2018).
33. A. D. Ruíz Pérez, et al., “In situ study of porous silicon thin films thermal oxidation by pulsed laser photoacoustics,” Semicond. Sci. Technol. **33**, 085001 (2018). doi: 10.1088/1361-6641/aacbe4
34. M. B. de la Mora, et al. Porous silicon photoluminescence modification by colloidal gold nanoparticles: Plasmonic, surface and porosity roles, J. Luminescence **146**, 247-255 (2014). doi: 10.1016/j.jlumin.2013.09.053
35. S. Escobar, et al. Light polarization in active photonic waveguides of porous silicon, PNFA **3**1, 44-51 (2018). doi: 10.1016/j.photonics.2018.05.009
36. M. B. de la Mora, et al. Porous silicon biosensors State of the Art in Biosensors – General Applications. Ed. T. Rinken (Rijeka: InTech). Chapter 6
37. A. D. Ruiz-Pérez, J.-A. Reyes-Esqueda, “Generalization of microcavities: Effects of asymmetry in the field localization and transmittance for supported microcavities,” PNFA **45**, 100915 (2021). doi: 10.1016/j.photonics.2021.100915

38. A. D. Ruiz-Pérez, S. Escobar, R. Nava, and J.-A. Reyes-Esqueda, “Room-temperature polariton repulsion and ultra-strong coupling for a non-trivial topological one-dimensional tunable Fibonacci-conjugated porous-Silicon photonic quasi-crystal showing quasi bound-states-in-the-continuum,” arXiv:2305.10532v2 [physics.optics]
39. Z. Cheng, H. Jiang, X. Zhang, F. Cheng, M. Wu, and H. Zhang, “Fundamental understanding and facing challenges in structural design of porous Si-based anodes for lithium-ion batteries,” Adv. Funct. Mater. **33**, 202301109 (2023). doi: 10.1002/adfm.202301109
40. A.G. Cullis, L.T. Canham, and P.D.J. Calcott, “The structural and luminescence properties of porous silicon,” J. Appl. Phys. **82**, 909–965 (1997). doi: 10.1063/1.366536
41. M. Born and E. Wolf. Principles of Optics, 6th edition, London: Pergamon 1980.
42. C. F. Klingshirn, “Semiconductor Optics,” 4th edition, Graduate Texts in Physics, Springer-Verlag Berlin Heidelberg 2012. doi: 10.1007/978-3-642-28362-8.
43. P. Xie, et al. “Strong light-matter interactions in hybrid nanostructures with transition metal dichalcogenides,” J. Opt. **24**, 093001 (2022). doi: 10.1088/2040-8986/ac8493.
44. Y. M. Qing, et al. “Strong coupling in two-dimensional materials-based nanostructures: a review,” J. Opt. **24**, 024009 (2022). doi: 10.1088/2040-8986/ac47b3.
45. A. Dutta, S. K. Dutta, S. D. Adhikari, and N. Pradhan, “Tuning the size of $CsPbBr_3$ nanocrystals: all at one constant temperature,” ACS Energy Lett. **3**(2), 329-334 (2018). doi: 10.1021/acsenergylett.7b01226.
46. D. Estrada-Wiese and J. A. del Río. Refractive index evaluation of porous silicon using bragg reflectors, Revista Mexicana de Física **64**, 72–81 (2018). doi: 10.31349/RevMexFis.64.72.
47. M. Araujo and P. Sacramento, “Topology in Condensed Matter. An introduction,” 1st edition, Singapore: World Scientific Publishing Co. Pte. Ltd. 2021. doi: 10-1142/12286#t=suppl.
48. X. Xie, et al. “Topological cavity based on slow-light topological edge mode for broadband Purcell enhancement,” Phys. Rev. Appl. **16**, 014036 (2021). doi: 10.1103/PhysRevApplied.16.014036.
49. D. C. Marinica and A. G. Borisov, “Bound state in the continuum in photonics,” Phys. Rev. Lett. **100**, 183902 (2008). doi: 10.1103/PhysRevLett.100.183902.
50. N. Fernández-García, E. Hernández, A. Jáuregui, and A. Mondragón, “Bound states at exceptional points in the continuum,” J. Phys: Conf. Series **512**, 012023 (2014). doi: 10.1088/1742-6596/512/1/012023.
51. F. H. Stillinger and D. R. Herrick, “Bound states in the continuum,” Phys. Rev. A **11**(2), 446-454 (1975). doi: 10.1103/PhysRevA.11.446.
52. C. M Bender, “PT Symmetry In quantum and classical physics,” Ch. 1, 1st Ed., World Scientific (2019). doi: 10.1142/q0178.
53. Ch. Li, R. Yang, X. Huang, Q. Fu, Y. Fan, and F. Zhang, “Experimental demonstration of controllable PT and anti-PT coupling in a non-Hermitian metamaterial,” Phys. Rev. Lett. **132**, 156601 (2024). doi: 10.1103/PhysRevLett.132.156601.
54. J. Qian, J. Li, Sh.-Y. Zhu, J. Q. You, and Y.-P. Wang, “Probing PT-Symmetry breaking of non-Hermitian topological photonic states via strong photon-magnon coupling,” Phys. Rev. Lett. **132**, 156901 (2024). doi: 10.1103/PhysRevLett.132.156901.
55. R. W. Boyd, “Nonlinear Optics,” Ch. 6, 3rd Ed., Academic Press (2008).
56. S. H. Autler and C. H. Townes, “Stark effect in rapidly varying fields,” Phys. Rev. **100**(2), 703-722 (1955). doi: 10.1103/PhysRev.100.703.
57. B. R. Mollow, “Power spectrum of light scattered by two-level systems,” Phys. Rev. **188**, 1969-1975 (1969). doi: 10.1103/PhysRev.188.1969.
58. H-X. Wang and J-H. Jiang, “A short review of all-dielectric topological photonic crystals,” Front. Phys. **10**, 866552 (2022). doi: 10.3389/fphy.2022.866552.
59. G. Xie, Z. Li, T. Luo, H. Bai, J. Sun, Y. Xiao, L.-D. Zhao, J. Wu, G. Tan, and X. Tang, “Band inversion induced multiple electronic valleys for high thermoelectric performance of SnTe with strong lattice softening,” Nano Energy **69**, 104395 (2020). doi: 10.1016/j.nanoen.2019.104395.